Available online at www.sciencedirect.com

ScienceDirect

Acta Materialia 63 (2014) 191–201

Acta MATERIALIA

www.elsevier.com/locate/actamat

Relation between thermolectric properties and phase equilibria in the $ZnO–In_2O_3$ binary system

Xin Liang *, David R. Clarke

School of Engineering and Applied Sciences, Harvard University, Cambridge, MA 02138, USA

Received 24 July 2013; accepted 15 October 2013
Available online 9 November 2013

Abstract

The electrical conductivities, Seebeck coefficients and thermal conductivities across the $ZnO–In_2O_3$ binary system are reported and related to the phase compositions and microstructures present at 1150 and 1250 °C. The $ZnO–In_2O_3$ binary system is of particular interest as it contains a variety of different types of phases, superlattice (modular) phases, solid solutions, two-phase regions and crystallographic features. Throughout much of the phase diagram, the thermal conductivities are less than 2 W m^{-1} K^{-1}, being limited by both solid solution disorder and thermal resistance due to the presence of InO/ZnO interfaces. Across the phase diagram, irrespective of the actual phases, the materials behave at high temperatures (800 °C) as free-electron conductors with the Seebeck coefficient and electron conductivity satisfying the Jonker's relationship. In the two-phase regions of the phase diagram, the values of the power factor and figure of merit (ZT) are consistent with a simple law of mixtures, weighted according to the volume fractions of the two phases. Although the largest values of electrical conductivity and Seebeck coefficient occur over a range of composition centered at 40 m/o $InO_{1.5}$, the maximum ZT and power factors are observed at $k = 4$ (33 m/o $InO_{1.5}$). In contrast to the other modular phases at 1250 °C and below, this phase is hexagonal rather than rhombohedral.
Published by Elsevier Ltd. on behalf of Acta Materialia Inc.

Keywords: Thermoelectrics; Oxide; Microstructure; Superlattice; Two-phase materials

1. Introduction

Studies of the thermoelectric properties of materials are usually restricted to a single composition or compound of interest and report on the effect of variables, such as doping concentration [1–8], processing or grain size [9]. While such studies are essential once a promising material has been identified and provide invaluable information, they do not include the effect of compositional changes with the exception of simple solid solutions, for instance silicon–germanium [10]. In contrast, in this work we investigate the thermoelectric properties over the full compositional range of the $ZnO–In_2O_3$ binary system in order to explore systematic variations with composition. This oxide material system is of interest as the basis for high-temperature thermoelectrics [11–15] and because it exhibits a range of possible phases and microstructures [16]. These range from the pure compounds, simple solid solutions, two-phase regions and modular or natural superlattice (SL) compounds [17], as well as solid solution phases containing planar interfaces. This unusual variety provides an opportunity to quantify the effects of point defect scattering and interface scattering as well as phase content on the thermal and electrical conductivity, all within the same system. Investigation of the two-phase compositions also enables us to compare with the mean-field predictions of the thermoelectric properties of two-phase polycrystalline materials.

The thermal-to-electrical efficiency of thermoelectrics, η, is usually given in terms of a non-dimensional figure of merit, ZT:

* Corresponding author. Tel.: +1 617 496 4295.
E-mail address: xinliang@fas.harvard.edu (X. Liang).

1359-6454/$36.00 Published by Elsevier Ltd. on behalf of Acta Materialia Inc.
http://dx.doi.org/10.1016/j.actamat.2013.10.027

$$\eta = \frac{T_H - T_C}{T_H}\left(\frac{(1+ZT)^{\frac{1}{2}}-1}{(1+ZT)^{\frac{1}{2}}+T_C/T_H}\right) \quad (1)$$

where T_H and T_C are temperatures at the hot and cold sides, respectively. The thermoelectric figure of merit ZT can be expressed in terms of the thermal conductivity κ, Seebeck coefficient S and electronic conductivity σ by the relationship:

$$ZT = \frac{S^2\sigma}{\kappa}T \quad (2)$$

where the numerator term $S^2\sigma$ is defined as the thermoelectric power factor (PF). The difficulty in identifying promising thermoelectric materials is that these properties are not independent of one another. Furthermore, as illustrated by the graphs in the review by Snyder and Toberer [18], variations in them are sometimes contra-indicated. However, since the thermal conductivity is in the denominator it is often used as an initial screening parameter. It is also the easiest to estimate from existing models. For these reasons, there has been considerable attention given to microstructural modification, such as reduction in grain size, in order to decrease thermal conductivity of thermoelectric materials. In this work, we will quantify the effect of each of the parameters in Eq. (2). The majority of the results presented will be those measured at 800 °C since these materials are primarily of interest as thermoelectrics at high temperatures in oxidizing atmospheres.

2. The $ZnO–In_2O_3$ binary

To provide a guide to the phases and compositions studied, the principal features of the $ZnO–In_2O_3$ binary in air are briefly reviewed using the phase diagram in Fig. 1, reproduced from the work of Moriga et al. [16]. In addition to the two terminal compositions, ZnO and $InO_{1.5}$, there is a series of single phase, line compounds whose compositions are given by the formula $In_2O_3(ZnO)_k$, where k is an integer. These compounds, sometimes referred to as modular compounds, or superlattice compounds, consist of a homologous series of alternating ZnO and In_2O_3 blocks, stacked along the c-axis direction of the ZnO wurtzite crystal structure, where k is the number of ZnO layers between each InO_2 layer. There remains some uncertainty about the detailed atomic arrangement of these compounds but all of them can be considered to consist of superlattices of individual InO_2 layers periodically interspersed within ZnO. Starting at the ZnO end of the phase diagram, the microstructure consists of a single phase solid solution of randomly distributed In^{3+} ions up until ~10 m/o and 5 m/o $InO_{1.5}$ at 1150 °C and 1250 °C, respectively. With increasing indium concentration, pseudo-randomly distributed InO_2 layers form within ZnO grains. These InO_2 layers are crystallographically also inversion domain boundaries (IDBs) on account of the symmetry inversion that occurs across them. (Similar inversion domain boundaries have been reported in Sb-doped ZnO [19] and in ZnO-based varistors [20].)

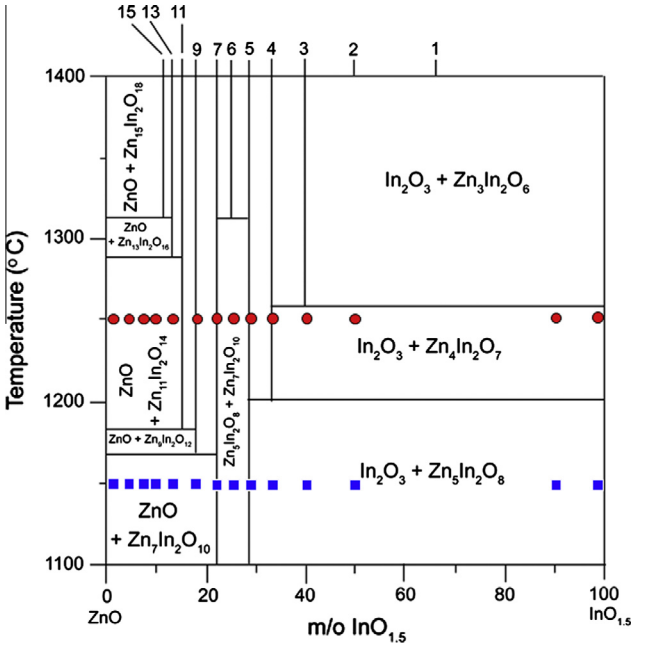

Fig. 1. The compositions of the materials studied superimposed on the $ZnO–In_2O_3$ binary phase diagram [16]. Two sets of materials were annealed at 1150 °C for 1 day (circles) and at 1250 °C for 7 days (squares). Phase regions of interests include In_2O_3-rich two-phase regions, the two-phase regime of $In_2O_3(ZnO)_5$ and $In_2O_3(ZnO)_7$ modular compounds, and the ZnO solid solution phase with individual InO_2 interfaces. In this and subsequent diagrams, the superlattice repeat value, k, is indicated along the top axis for phases stable below 1300 °C.

Starting with pure ZnO, the first single-phase modular compound forms at $k = 7$ (22 m/o $InO_{1.5}$) at 1150 °C and $k = 9$ at 1250 °C and then there is a series of modular compositions, each distinguished by a discrete k value. The compounds are rhombohedral when the k values are odd. The phase diagram indicates that different compounds are stable over different ranges of temperature and that the higher the temperature the greater the number of equilibrium modular compounds. In between the line compounds, there are, notionally at least, two-phase coexistence regions consisting of a mixture of two modular compounds. At the In_2O_3-rich portion of the diagram the two-phase regions consist of a mixture of In_2O_3 and a modular compound whose composition depends on the temperature.

In this work we report on the properties of materials heat-treated in air at either 1150 °C for 1 day or 1250 °C for 7 days; the compositions of samples synthesized and investigated are indicated in Fig. 1. Based on our preliminary measurements, these two temperatures are sufficient to create stable microstructures. Annealing at higher temperature is possible but the increased volatility of both Zn and In makes it more difficult to ensure compositional homogeneity within samples.

3. Experimental details

A series of compositions across the $ZnO–In_2O_3$ binary phase diagram was prepared from high purity nitrate

powders, $Zn(NO_3)_2$ (99.999%, Sigma Aldrich®, USA) and $In(NO_3)_3$ (99.999%, Sigma Aldrich®, USA), dissolved in deionized and distilled water. Specific compositions were made by mixing appropriate nitrate solutions and heating them at 80 °C. Several organic fuels (acrylamide, N,N′-methylene-bisacrylamide, 2,2′-azobisisobutyro-nitrile and ammonium persulfate) were then mixed in converting the solutions into gels. They were then dried in the low temperature drying oven at 120 °C for 12 h before grinding into fine particles and combusted by heating at 600 °C. The remaining mixture of oxide and carbon powders was then calcined at 825 °C for 2 h to remove the residual carbon and other organic chemicals. The powders are then sintered into solid pellets 12.7 mm in diameter and 1–1.5 mm in thickness using current assisted densification processing system (also known as spark plasma sintering) at 900 °C for 5 min at a constant pressure of 125 MPa. After the densification, the samples were annealed in air at 900 °C for 2 h to restore the oxygen stoichiometry. The samples were then annealed at either 1150 °C for 1 day or 1250 °C for 7 days in order to achieve different phase equilibria and microstructures. To avoid evaporation of ZnO and In_2O_3, each of the sample pellets was embedded in oxide powders of the same compositions in a covered crucible. To serve as a reference, pellets of pure ZnO were made in the same way and annealed at 1150 °C for 1 day to fully oxidize the material.

X-ray diffraction analysis was performed with a Philips® PANalytical Multipurpose Diffractometer and the phases identified using PANalytical X'Pert HighScore Plus software connected to the 2011 ICDD PDF database [21]. To investigate the grain size and microstructure, the cross-sections of selected samples were ground and polished down to 1 μm, and were then thermally etched at 1050 °C for 30 min. Scanning electron microscopy imaging and elemental mapping were performed on a Zeiss® Super VP55 field emission gun scanning electron microscope (FEG-SEM) with an energy dispersive X-ray spectrometer (EDS). High-resolution transmission electron microscopy (HRTEM) imaging and diffraction analysis were also carried out on selected samples to observe the detailed structures. Specimens for TEM observations were first thinned by polishing both sides until the thickness was reduced down to ~60–80 μm, and then thinned to electron transparency by ion-beam milling using a Fischione® 1010 Dual Beam Ion-Mill. After plasma cleaning in a Fischione® 110 Plasma Cleaner the samples were examined using a JEOL 2100 TEM and JEOL 2010 FEG-TEM.

The thermal conductivity (κ) was determined from the thermal diffusivity using the standard relationship:

$$\kappa = \alpha \cdot \rho \cdot C_p \tag{3}$$

The diffusivity (α) was measured from room temperature to 800 °C in flowing argon gas using the laser flash method (NETZCH Micro Flash® LFA 457) equipped with a 1.06 μm laser with a (350 μs) pulse. The heat capacities for each composition, C_p, were calculated using the Kopp–Neumann rule from literature data [22] and the mass density ρ measured using the Archimedes method. The electrical conductivity and Seebeck coefficient were measured in air from room temperature to 800 °C on polycrystalline bars of dimensions $2 \times 2 \times 8$ mm using a ULVAC RIKO® ZEM 3 M10 unit.

4. Observations and results

In this section, the electrical and thermal transport properties across the ZnO–In_2O_3 binary system are presented and related to the phase content and microstructures in the principal regions in the equilibrium phase diagram. The data are summarized in Figs. 2–5 for samples annealed at either 1150 °C for 1 day or 1250 °C for 7 days. Figs. 2 and 3 show the thermal conductivity against indium concentration measured at room temperature and 800 °C, respectively. Perhaps the most striking feature of the data is that the thermal conductivity is relatively independent of indium concentration above ~10 m/o $InO_{1.5}$. Figs. 4 and 5 report the electrical conductivity and Seebeck coefficient as a function of indium concentration measured at 800 °C, respectively. As can be seen from Fig. 5, the Seebeck coefficient is negative across the phase diagram, indicating that all the compounds are *n*-type semiconductors.

4.1. ZnO solid solution compositions

For the indium concentrations up to 8 or 10 m/o $InO_{1.5}$ (at 1150 °C), the phase diagram indicates that the material is a solid solution consisting of indium ions dissolved in ZnO. Our microscopy is consistent with this expectation and the microstructure is featureless with a grain size of a few hundred nm. Over this solid solution region, the

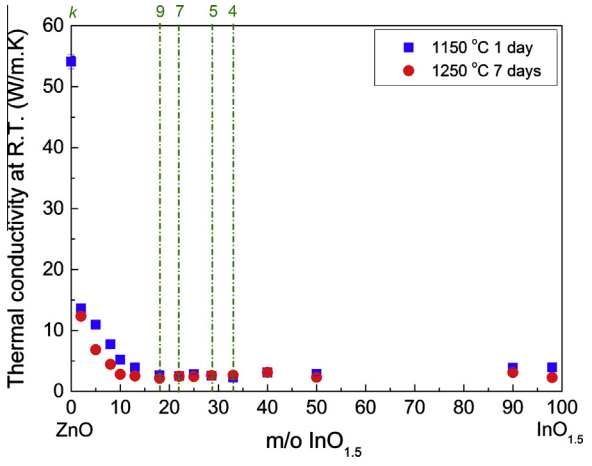

Fig. 2. RT thermal conductivity as a function of indium concentration for samples heat-treated at either 1150 °C for 1 day (blue squares) or 1250 °C 7 days (red filled circles). In this and succeeding figures the compositions of the modular superlattice compounds $k = 4, 5, 7, 9$ stable below 1300 °C are indicated by the vertical dashed lines. (For interpretation of the references to color in this figure legend, the reader is referred to the web version of this article.)

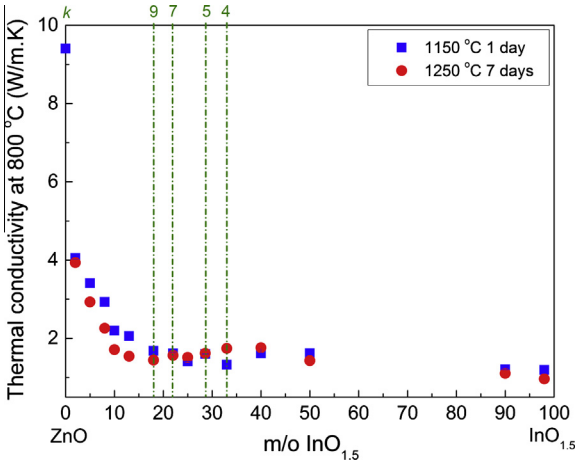

Fig. 3. Thermal conductivity at 800 °C, for two sets of thermal treatments, 1150 °C 1 day (blue squares) and 1250 °C 7 days (red circles), respectively. (For interpretation of the references to color in this figure legend, the reader is referred to the web version of this article.)

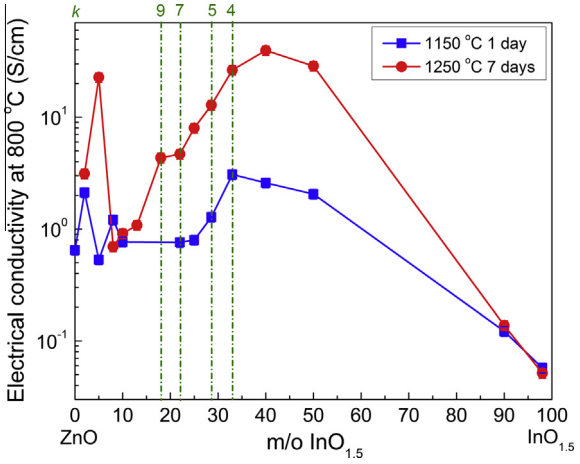

Fig. 4. Electrical conductivity of $ZnO–In_2O_3$ oxide system as a function of indium concentration. Data presented are measurements made at 800 °C. The lines through the data points are guides to the eye.

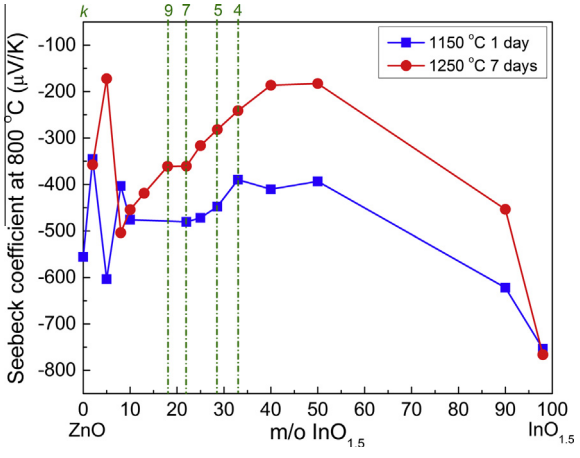

Fig. 5. Seebeck coefficient at 800 °C as a function of indium concentration.

thermal conductivity rapidly decreases with increasing indium concentration from a room temperature value of 54 W m^{-1} K^{-1} for the fully densified pure material to less than 5 W m^{-1} K^{-1}. The electrical conductivity and Seebeck coefficient also increase with increasing indium concentration in this compositional range after annealing at 1150 °C for 1 day. The increase in electrical conductivity with doping is consistent with the effect of other aliovalent dopants, such as Al^{3+} and Ga^{3+} in ZnO [1–3,23–25]. The one notable exception is the unusually high conductivity of the 5 m/o $InO_{1.5}$ annealed for 7 days at 1250 °C, a very reproducible finding.

4.2. ZnO solid solution containing planar crystallographic interfaces

For indium concentrations above ~ 10 m/o $InO_{1.5}$ annealed at 1150 °C and above ~5 m/o $InO_{1.5}$ annealed at 1250 °C, the solid solubility is exceeded and planar interfaces form on the basal plane of the ZnO grains. As remarked earlier these are believed to consist of individual InO_2 planes. An example is shown in Fig. 6a of the 10 m/o $InO_{1.5}$ material after 1 day at 1150 °C. The superlattice structures are clearly seen but the interface spacing is apparently not constant. This is a common feature of these and other polytype homologous compounds, as has been reported previously [26–29] and is attributed to the weak interaction between the InO_2 planes and slow kinetics required for long-range diffusion.

With further increasing indium concentration (from 10 up to 22 m/o $InO_{1.5}$), modular compounds become stable and appear in the solid solution phase of the phase diagram as planar interfaces associated with inversion domain boundaries. After higher temperature annealing (1250 °C for 7 days), however, the structure of each grain evolves into a “chessboard pattern” that essentially consists of two sets of intersecting interfaces within the same grain, as shown in Fig. 6b.

The thermal conductivity of the solid solution phases containing InO_2 planes decrease with increasing indium concentration, at both room temperature (Fig. 2) and 800 °C (Fig. 3). However, the thermal conductivity becomes almost constant with indium concentration above ~18 m/o $InO_{1.5}$. Furthermore, it is also found that thermal conductivity becomes much less temperature-dependent as compared to the simple solid solution microstructure; the conductivity over the full temperature range (room temperature (RT) to 800 °C) has been published elsewhere [30]. Electrical conductivity in this phase region demonstrates slightly different dependence on indium concentration for two series of thermally treated samples, as shown in Fig. 4. The electrical conductivity of the 1150 °C series sample is relatively constant with indium concentration whereas that of the 1250 °C series sample increases with indium addition. The dependence of the Seebeck coefficient on the indium concentration has an opposite trend to that of electrical conductivity, as shown in Fig. 5.

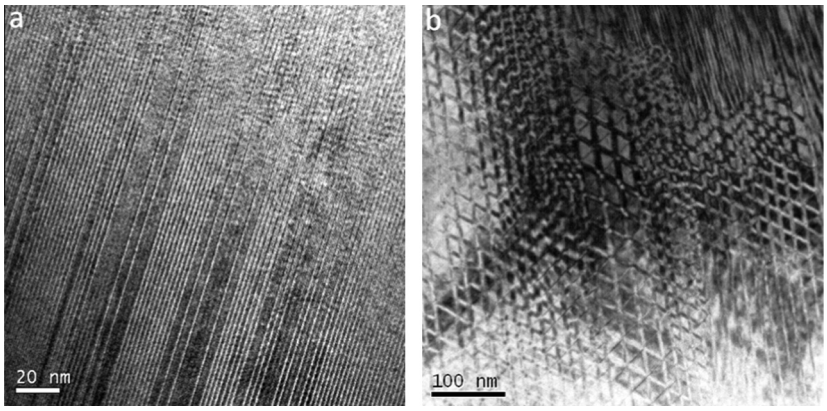

Fig. 6. TEM micrographs of 10 m/o $InO_{1.5}$, after post-annealing for (a) 1150 °C for 1 day and (b) 1250 °C for 7 days (b). The latter has a "chessboard" type pattern consisting two sets of superlattice structures of InO_2 sheets.

4.3. The modular compounds

The modular phases formed were as expected from the phase diagram. At 1150 °C the single-phase modular compound formed at $k = 7$ and at 1250 °C the stable modular compound formed at a smaller indium concentration, $k = 9$. High resolution microscopy indicated a well-ordered superlattice structure, as shown in Fig. 7 for the $k = 7$ (22 m/o $InO_{1.5}$). Selected area diffraction patterns (presented in the inset) exhibited sharp, regular superlattice spots, again indicative of a well-ordered structure. Together with X-ray diffraction (XRD) (not shown), this indicates that the $k = 7$ and $k = 9$ are largely single-phase compounds. In contrast, the modular compounds $k = 5$ and $k = 4$ consisted of mixed modular compounds.

4.4. Indium-rich two-phase regions

Consistent with the indium-rich end of the phase diagram, two different two-phase regions were found over the temperature range considered: (1) an In_2O_3 two-phase region and (2) the two superlattice compound mixture regions ($k = 5$ and 7). The 50 m/o $InO_{1.5}$ material annealed at 1250 °C was identified by XRD as a two-phase mixture consisting of In_2O_3 and the $In_2O_3(ZnO)_4$ compound. It has a typical microstructure consisting of two discrete phases, as shown in Fig. 8a. Elemental mapping reveals, as expected, indium-rich grains and a second, indium-poor phase (Fig. 8b). The indium-poor phase is $In_2O_3(ZnO)_4$ (the $k = 4$ phase). The proportion of the two phases is consistent with the Lever rule on the phase diagram at 1250 °C.

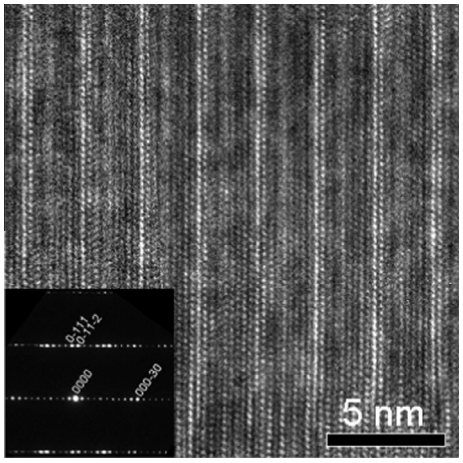

Fig. 7. HRTEM image of 22 m/o $InO_{1.5}$ after post-annealing for 1150 °C for 1 day, showing the almost constant superlattice spacing; the inset is the selected area diffraction pattern taken with zone axis $\langle 10\bar{1}0 \rangle$, where superlattice reflection spots are clearly captured. Both HRTEM image and indexing of the diffraction pattern confirm the observed structure as the $In_2O_3(ZnO)_k$ phase.

In the In_2O_3-rich two-phase regions, the thermal conductivities were in the range of 2–3 $W\,m^{-1}\,K^{-1}$ at room temperature and were relatively constant with increasing indium concentration. Electrical conductivity increases monotonically with the fraction of second phase ($In_2O_3(ZnO)_4$ or $In_2O_3(ZnO)_5$) while, again, the Seebeck coefficient has the opposite dependence. High temperature annealing was found to significantly increase the electrical conductivity. In the region consisting of a mixture of two modular compounds, $k = 5$ and 7, i.e. $0.25 \leqslant InO_{1.5} \leqslant 0.33$, the thermal conductivity also remained almost constant, as shown in Figs. 2 and 3. Electrical conductivity in this region increased with indium concentration or the fraction of $In_2O_3(ZnO)_5$ compound, as seen in Fig. 4. In addition, the electrical conductivity of the 1250 °C series samples was about one order of magnitude larger than those annealed at 1150 °C.

5. Discussion

The data presented indicate that, although the electrical conductivity and Seebeck coefficient exhibit large variations with indium concentration across the binary compositional range, the thermal conductivity is relatively independent once there is sufficient indium to form InO_2 sheets. To understand these contrasting behaviors we first discuss the variation in thermal conductivity in terms of the microstructures characteristic of the different phases in the ZnO–In_2O_3 system. This is then followed by a discussion of the electrical transport properties. Together, these

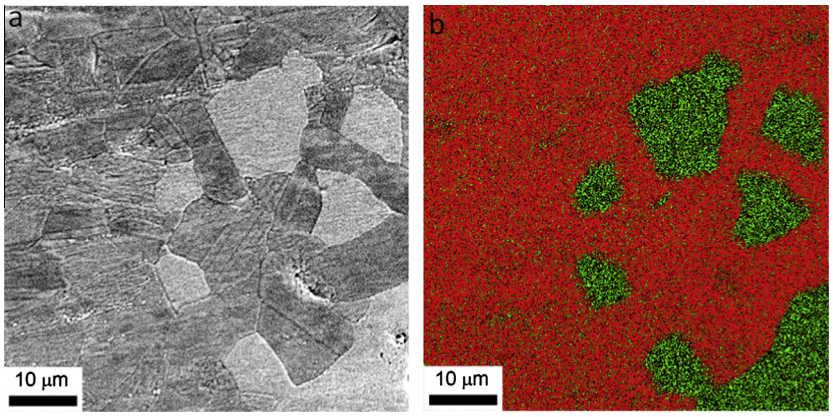

Fig. 8. SEM image and elemental mapping of the cross-section microstructure of the 50 m/o $InO_{1.5}$ after 1250 °C 7 days' annealing: (a) SEM micrograph revealing the grain microstructure. (b) The corresponding EDS mapping showing the distribution of zinc (red) and indium (green). (For interpretation of the references to color in this figure legend, the reader is referred to the web version of this article.)

set the stage for understanding the variation of the thermoelectric power factor and figure of merit with composition. Before doing this, though, we estimate the electronic contribution to the thermal conductivity using the Wiedemann–Franz relationship:

$$\kappa_e = L\sigma T \tag{4}$$

where κ_e is the electronic contribution to the thermal conductivity and L is the Lorentz factor, typically 2.0×10^{-8} $J^2\,K^{-2}\,C^{-2}$ for degenerate semiconductors [31]. Taking the highest value of the electrical conductivity measured, $\sim$40 S cm^{-1} at 800 °C for 40 m/o $InO_{1.5}$, the electronic thermal conductivity is calculated to be $\kappa_e \approx 0.08$ W m^{-1} K^{-1}. This is more than an order of magnitude smaller than the thermal conductivities measured, indicating that it is negligible compared to the lattice contribution to the phonon thermal conductivity. Based on this estimate, the following discussions of thermal conductivity are couched in terms of phonon scattering mechanisms alone.

5.1. ZnO solid solution region: point defect phonon scattering

The rapid decrease in thermal conductivity with indium addition in the solid solution phase region is indicative of strong point defect scattering of phonons by indium ions substituting into the ZnO lattice. At temperatures above the Debye temperature, the thermal conductivity of crystalline materials can be expressed as:

$$\kappa = \frac{k_B\sqrt{v_s}}{\sqrt{\pi^3}}\frac{1}{\sqrt{\Omega_0 C\Gamma}}\frac{1}{\sqrt{T}}\tan^{-1}\left(\frac{k_B\theta}{\hbar}\left(\frac{\Omega_0\Gamma}{4\pi v_s^3 CT}\right)^{\frac{1}{2}}\right) + \kappa_{min} \tag{5}$$

where the first term is the Callaway–van Baeyer description [32] of the effect of defect concentration and temperature on thermal conductivity and the second term is the high-temperature limit κ_{min} when the phonon wavelength approaches the interatomic distance [33–35]. k_B is Boltzmann's constant, v_s the sound velocity and Ω_0 is the unit cell volume. The constant C is the inverse time coefficient for phonon–phonon scattering processes in pure ZnO and is obtained by fitting Eq. (5) to the temperature dependence of pure ZnO. Γ is the phonon scattering strength of the point defects introduced by indium solid solution alloying. Indium is known to be a substitutional solute in ZnO, substituting for the Zn ion and creating cation vacancies for site and charge balance according to the overall defect reaction [36]:

$$In_2O_3 \overset{ZnO}{\rightarrow} [In_{Zn}^{\cdot} : V_{Zn}'' : In_{Zn}^{\cdot}]^X + 3O_O^X + 3ZnO \tag{6}$$

Writing the indium concentration as c, the formula for indium-doped ZnO can be expressed as:

$$\left(Zn_{1-\frac{3}{2}c}In_cV_{\frac{c}{2}}\right)O \tag{7}$$

In turn, the phonon scattering parameter Γ can be written as the mass variance on the cation site only since there are no defects on the anion lattice:

$$\Gamma = \frac{1}{2}\left(\frac{M_{Zn}}{\overline{M}}\right)^2\Gamma(A) = \frac{1}{2}\left(\frac{M_{Zn}}{\overline{M}}\right)^2\frac{\sum_j f_j(M_j - \overline{M_{Zn}})^2}{(\overline{M_{Zn}})^2} \tag{8}$$

where the summation is over the two different types of point defect, the substitutional and vacancy defects. To a first order approximation in indium doping concentration,

$$\Gamma \approx 1.38c \tag{9}$$

Consistent with the data shown in Figs. 2 and 3, the conductivity κ decreases with indium concentration, c.

5.2. ZnO solid solution containing planar interfaces

When the indium concentration exceeds its solid solubility in ZnO, our microscopy data, as well as those of others [36,37], indicates that one-dimensional (1-D) superlattice structures consisting of InO_2 planes inserted in the ZnO structure are formed. Their effect is to introduce additional phonon scattering, reducing the phonon mean free path while also introducing thermal conductivity anisotropy parallel and perpendicular to the InO_2 planes. The thermal

conductivity of the ZnO solid solution containing these planar interfaces can then be written as:

$$\frac{1}{\kappa} = \frac{1}{\kappa_i} + \frac{R_k}{d_{SL}} \tag{10}$$

where κ_i is the thermal conductivity of the materials with point defects and the second term is the contribution of the thermal resistance associated with the InO/ZnO interfaces. d_{SL} is the average interface spacing which depends on the indium concentration, and is given by the following relation:

$$d_{SL} \approx (k+1) \times d_{\{0002\}} \tag{11}$$

where $d_{\{0002\}}$ is the basal plane spacing of the ZnO lattice (0.260 nm for pure ZnO). Accordingly, as the indium concentration increases, the interface density increases and the spacing d_{SL} decreases, leading to a reduction in thermal conductivity. Detailed analysis of the indium concentration and temperature dependence of this contribution to thermal conductivity has recently been quantified [30] and the important finding for this work is that the InO/ZnO interface is estimated to have a thermal (Kapitza) resistance R_k of $5.0 \pm 0.5 \times 10^{-10}$ m^2 K W^{-1}.

Our microscopy observations indicate that after annealing at the higher temperature (1250 °C), a complex "chessboard" of intersecting InO_2 planes forms, as shown in Fig. 6b. The effect of such intersecting faults on thermal conductivity has not been modeled in the literature. However, at the simplest level, one can assume that the InO/ZnO interfaces formed have the same thermal resistance as in the 1-D superlattice structures. Further, as they are arranged on different crystallographic planes, they will decrease the thermal conductivity anisotropy, further lowering the overall thermal conductivity. Lacking a detailed model, this would qualitatively cause a reduction in thermal conductivity of the materials annealed at 1250 °C relative to the same compositions annealed at 1150 °C. This is seen when the data measured at both room temperature and 800 °C are compared (Figs. 2 and 3).

5.3. Modular compounds

As shown in Figs. 2 and 3, the thermal conductivities of the modular $In_2O_3(ZnO)_k$ compounds ($k = 4, 5, 7, 9$) are similar, being in the range of 2–3 W m^{-1} K^{-1} at room temperature and 1.25–2.1 W m^{-1} K^{-1} at 800 °C. Since they only differ structurally by the spacing of the InO_2 planes, their thermal conductivities can be estimated from the spacing between the InO_2 planes and the thermal resistance of the InO/ZnO interface using Eqs. (10) and (11). For example, when the periodicity of the InO_2 layers in the $k = 7$ compound, $In_2O_3(ZnO)_7$, is used, the thermal conductivity is calculated to be 2.3 W m^{-1} K^{-1}, very close to the measured value of 2.5 W m^{-1} K^{-1}. Repeating the calculation for the other modular compounds, the estimated values are close to those reported as summarized in Table 1.

5.4. Electrical transport properties

The most striking feature of the data in Figs. 4 and 5 is that the electrical conductivity and Seebeck coefficient exhibit opposite trends with indium concentration. This behavior is consistent with the correlation between the Seebeck coefficient and electrical conductivity of a free electron semiconductor with a density of states at the conduction band edge, N_c:

$$S = -\frac{k_B}{e}\left[\ln\left(\frac{N_c}{n}\right) + A\right] \tag{12}$$

where $N_c = \left(\frac{2\pi m_e^* k_B T}{\hbar^2}\right)^{\frac{3}{2}}$, A is a transport constant that depends on the electron scattering mechanism and typically has a value in the range of 0–4 and where m^* is the effective mass of the electrons, n is the number of carriers and μ is the mobility:

$$\sigma = ne\mu \tag{13}$$

Consistent with these expectations is that the higher conductivities measured on the materials annealed at 1250 °C are reflected by systematically lower values of the Seebeck coefficient. The one significant outlier is the data at a concentration of 5 m/o $InO_{1.5}$ annealed at 1250 °C for 7 days. These data, which occur at the onset of the formation of InO_2 planes, are very reproducible, suggesting that there may be some unusual interactions effects with the InO_2 planes that we cannot explain.

The variation of the Seebeck coefficient with electron conductivity can also be represented by plotting the Seebeck coefficient as a function of the natural logarithm of electrical conductivity (a Jonker plot):

$$S = \frac{k_B}{e}(\ln(\sigma) - \ln(\sigma_0)) \tag{14}$$

where $\sigma_0 = N_c e\mu \exp(A)$. When our data, measured at 800 °C, are plotted this way across the full composition range of the ZnO–In_2O_3 phase diagram for both annealing conditions, a good correlation is obtained, as shown in Fig. 9. Furthermore, as indicated by the dashed line with a slope of +86.15 μV K^{-1}, corresponding to the value of k_B/e [31], the data are consistent with the Seebeck coefficient being determined by free electron transport in all the compositions. This is especially so for the materials annealed at 1250 °C. The intercept, $\ln(\sigma_0)$, sometimes referred to as the "DOS-μ" product, has a value of 10.0, similar to a recent assessment for some of the $In_2O_3(ZnO)_k$ phases [38]. So, while the microstructure affects the actual values of the conductivity, the evidence is that across the phase diagram each of the phases is a free-electron semiconductor.

Table 2 compares the electrical conductivity and Seebeck coefficient of the modular compounds studied in this work with values in the literature. One of the striking features of the electrical conductivity data is that they increase with the decreasing value of k (equivalently increasing indium concentration). In some cases, the conductivity is comparable to, if not exceeds, the conductivity of the

Table 1
Calculated RT thermal conductivity of $In_2O_3(ZnO)_k$ modular compounds based on InO/ZnO interface scattering (according to Eqs. (10) and (11)), together with the room temperature measurements in the present work (annealed at 1150 °C) and values reported in the literature.

k	Calculated values (RT)	Measured, present work (RT)	Literature (RT)
4	1.74	2.26	3.50 [44]
5	1.95	2.80	2.60 [14]; 3.45 [44]
7	2.31	2.49	3.95 [44]
9	2.6	2.65	2.65 [14]; 4.65 [44]

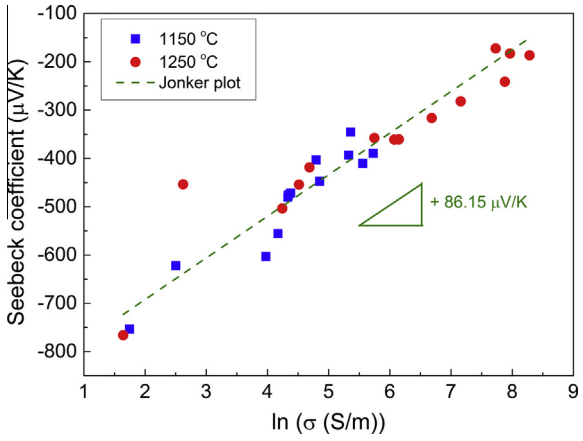

Fig. 9. Jonker plot (Seebeck coefficient against natural logarithm of electrical conductivity) of ZnO–In_2O_3 materials measured at 800 °C. The best fit of the data with a slope of +86.15 μV K^{-1} is shown as the dashed line.

doped ZnO. Also of interest is that the thermoelectric properties of these modular compounds monotonically increases with decreasing order of superlattice, i.e. the k value. Clearly seen in Figs. 10 and 11, both power factor and ZT increase almost linearly from $k = 9$ to 4. This may suggest that the low k compounds $In_2O_3(ZnO)_k$ are more electrically conducting, which is consistent with the findings in the literature that low k compound has large carrier concentration and mobility [16].

Apart from the variation in electrical conductivity with composition and the phase content, the other significant feature of the conductivity data is the consistently higher conductivities of the materials annealed for the longer time at higher temperature. This is attributed to the annealing out of point defects and local disorder at the higher temperature that reduce electron scattering. Indeed, in many of the previous studies that report higher electrical conductivities [27,39,40] the materials were annealed at higher temperatures and/or longer times. The effect on thermal conductivity is less striking but is nevertheless detectable at concentrations below which the modular compounds form. (At higher indium concentrations, the InO/ZnO interfaces are assumed to be more effective in phonon scattering and so the effect of annealing is less marked.).

5.5. Two-phase thermoelectrics in the indium-rich regions

The relative insensitivity of the thermal conductivity to indium concentrations greater than ~10 m/o $InO_{1.5}$, means that the thermoelectric figure of merit ZT and the thermoelectric power factor $S^2\sigma$ exhibit similar dependence on indium concentration. These trends are shown in Figs. 10 and 11. The data indicate that the compounds $k = 5$ (at 1150 °C) and $k = 4$ (at 1250 °C) have the largest values of both the thermoelectric power factor and ZT.

For compositions containing more indium than these compounds, the phase diagram, our XRD and our SEM and EDS analyses all indicate that the materials are two-phase. (There are also other two-phase regions consisting of mixtures of other modular compounds, albeit with a narrower range of composition, for instance between $Zn_7In_2O_{10}$ and $Zn_5In_2O_8$ compounds.) A striking feature of the data is that the power factor and figure of merit vary almost linearly with concentration between the two phases, suggesting that the thermoelectric properties obey the equivalent of the Lever rule, with the value being a weighted average of the volume fractions of the two phases. It is therefore of interest to compare our data with the mean field model presented by Bergman et al. [41,42] for the thermoelectric properties of a composite consisting of a randomly distributed mixture of two thermoelectric phases.

According to Bergman's model, the thermoelectric power factor of a random composite can be written in terms of the volume fraction, ϕ, and properties of the two phases, A and B, as:

Table 2
Electrical conductivity and Seebeck coefficient of $In_2O_3(ZnO)_k$ modular compounds measured at 800 °C, together with values reported in the literature.

k	Electrical conductivity (S cm^{-1})		Seebeck coefficient (μV K^{-1})	
	Present work	Literature	Present work	Literature
4	26.4	148 [44]	−241.2	−175 [44]
5	12.8	203 [12]; 98 [44]; 200 [51]	−281.7	−24 [12]; −193 [44]; −60 [51]
7	4.7	146 [12]; 70 [44]	−360.5	−42 [12]; −198 [44]
9	4.3	98 [12]; 65 [44]	−360.9	−82 [12]; −207 [44]

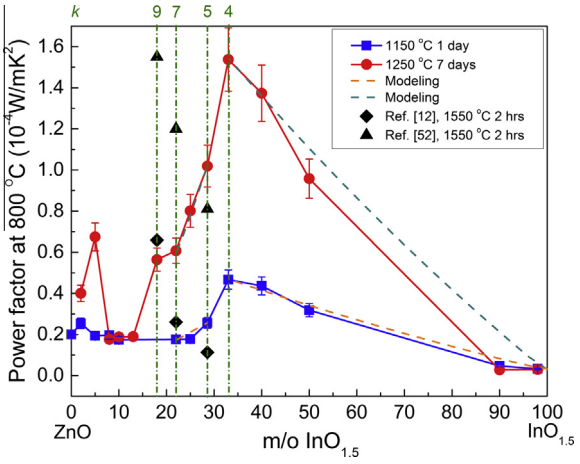

Fig. 10. Thermoelectric power factor at 800 °C after annealing at 1150 °C for 1 day (blue squares) and 1250 °C for 7 days (red circles). Also shown are literature measurements for the $k = 5$, 7, 9 compounds measured at 800 °C [12,51]. The dashed lines correspond to the Bergman effective medium model for two-phase thermoelectrics [41,42]. (For interpretation of the references to color in this figure legend, the reader is referred to the web version of this article.)

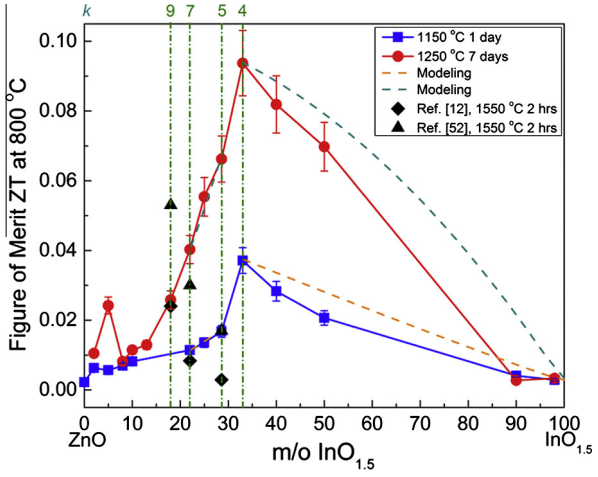

Fig. 11. Thermoelectric figure of merit at 800 °C. Also shown are values from the literature for the $k = 5$, 7, 9 compounds measured at 800 °C [12,51]. The dashed lines correspond to the Bergman effective medium model for two-phase composite thermoelectrics [41,42].

$$PF = \frac{[(1-\phi_B)(\sigma_A S_A - \sigma_B S_B) + \sigma_B S_B]^2}{(1-\phi_B)(\sigma_A - \sigma_B) + \sigma_B} \tag{15}$$

(In the Appendix, the volume fractions are computed from the molar phase fractions.) Fig. 10 compares the predictions of the model to our data at 1150 °C and 1250 °C for both the In_2O_3 and $Zn_4In_2O_7$ two-phase system and for the mixture of $Zn_7In_2O_{10}$ and $Zn_5In_2O_8$ superlattice compounds. Reasonable agreement is obtained.

The same mean field model can be applied to the thermoelectric figure of merit by including the variation in thermal conductivity with composition. For this purpose, we express the effective thermal conductivity of a two-phase composite, including the thermal resistance of the grain boundaries, derived by Nan et al. [43] as

$$\kappa = \kappa_A \frac{\kappa_B(1+2\alpha) + 2\kappa_A + 2\phi_B[\kappa_B(1-\alpha) - \kappa_A]}{\kappa_B(1+2\alpha) + 2\kappa_A - \phi_B[\kappa_B(1-\alpha) - \kappa_A]} \tag{16}$$

where κ is the effective thermal conductivity of the composite and κ_A and κ_B are the thermal conductivities of each component with ϕ_B the volume fraction of component B. The parameter α is a dimensionless parameter determined by the shape of the second component, assumed to be elliptical, as well as the interface (Kapitza) thermal resistance R_k. For spherical particles, α is the ratio of two characteristic lengths, the thermal width of the interface $R_k\kappa_m$ and the particle radius, a:

$$\alpha = \frac{R_k \kappa_m}{a} \tag{17}$$

where κ_m is the thermal conductivity of the matrix phase.

In order to estimate an appropriate value of α, we use the following values: the typical grain size of the second phase is ~5 μm based on our microscopy observations. The interfacial (Kapitza) thermal resistance R_k is $\sim 5.0 \times 10^{-10}$ m^2 K W^{-1} for InO/ZnO interfaces [30]. The thermal conductivities of In_2O_3 and $Zn_4In_2O_7$ at 800 °C are ~1.5 W m^{-1} K^{-1} and 2 W m^{-1} K^{-1}, respectively. Either of the phases could be the matrix phase depending on the indium concentration. Using these values, $\alpha \sim 10^{-3}$, meaning that the grain boundary thermal resistance can be neglected and the effective thermal conductivity can be written as:

$$\kappa = \kappa_A \frac{\kappa_B + 2\kappa_A + 2\phi_B(\kappa_B - \kappa_A)}{\kappa_B + 2\kappa_A - \phi_B(\kappa_B - \kappa_A)} \tag{18}$$

By combining the mean field expressions (Eqs. (15) and (18)) and evaluating them for the individual phases, the variation in figure of merit (Eq. (2)) over the two-phase regions is shown by the dashed lines in Fig. 11, for the 1150 °C and 1250 °C series, respectively. The experimental values for the figure of merit are again in reasonable agreement with the model, suggesting that Bergman's mean-field model is a reliable method of computing the thermoelectric properties of random two-phase mixtures.

5.6. Attaining compositional and structural homogeneity

As remarked upon earlier, there have been a number of previous studies of the thermoelectric properties of some of the modular compounds [12,14,44] as well as variously doped ZnO and In_2O_3 materials [1–3,19,23,25,45–50]. In comparing the results from the different studies, the largest variations are in the numerical values of the electrical conductivity and the smallest variations are in the thermal conductivities. The latter can be understood because the thermal conductivities are relatively insensitive to composition for indium concentrations >15 m/o $InO_{1.5}$ and are determined by phonon scattering from the InO/ZnO interfaces and solute scattering. Much of the reported variation in electrical conductivity can be attributed to the maximum temperature at which the materials have been equilibrated, annealing out extraneous point defects. Also related to

these variations in electrical conductivity, it is believed, are compositional and structural inhomogeneities. The formation of the modular compounds with well-defined periodicity requires long-range diffusion and the larger the k value the greater the distance over which diffusion must occur. Furthermore, if the temperature is changed, either during preparation of the materials or upon subsequent annealing, the kinetics of the change from one modular compound to another will also limit equilibration. One consequence of such kinetic limitations is that the lower temperature at which the modular compounds can form may be lower than indicated by the phase diagram in Fig. 1. A further consideration is that the modular compounds are line compounds and so it is difficult to make them single phase. For instance, Ohta et al. [12] measured the thermoelectric properties of the $k = 5, 7, 9$ compounds (sintered at 1550 °C for 2 h) from 250 to 800 °C and found that the figure of merit was significantly larger than pure ZnO due to the increase in electrical conductivity and decrease in thermal conductivity. However, the periodicity in some of their materials is obviously not constant, as shown in their TEM micrograph (e.g. their Fig. 2B). It is apparent that the properties they measured are those for a mixture of $In_2O_3(ZnO)_k$ compounds with varying k instead of a single one. We also note that our values systematically vary with indium concentration whereas Ohta's do not. It should also be noted that the difficulty in obtaining the single phase compounds has also been observed in other $RMO_3(ZnO)_k$ homologous structure systems [16,26–28,39]. Furthermore, in several papers, the reported value of k is the ratio between zinc and indium ions in the starting materials rather than in the final materials, and so do not account for compositional losses associated with the volatility of Zn and In.

6. Conclusions

The ZnO–In_2O_3 binary system has proven to be a good model system for relating thermoelectric properties, including thermal conductivity, to the various phases and compositional fields that exist at 1150 and 1250 °C. At low concentrations of indium (<10 m/o $InO_{1.5}$), the properties are relatively insensitive to the indium concentration except for the thermal conductivity that decreases very rapidly due to phonon scattering from substitutional indium ions. At higher concentrations, planar InO_2 sheets form and the thermal conductivity is almost independent of composition across the entire phase diagram at both 1150 and 1250 °C. At still higher indium concentrations, once modular compounds $In_2O_3(ZnO)_k$ form, the electrical conductivity and Seebeck coefficient depend on the k value, with the changes being more pronounced for the 1250 °C series than the 1150 °C series of compositions. The largest values of both power factor and ZT occur at a composition corresponding to the $k = 4$ compound, the only hexagonal compound in any of the compositional fields below 1320 °C. It is speculated that this is because this compound does not contain crystallographic interfaces where there is a reversal in polarization and consequently electrostatic barriers to electron transport across them.

At still higher indium concentrations, the materials are two-phase, consisting of In_2O_3 and a modular compound ($k = 5$ at 1150 °C and $k = 4$ at 1250 °C). In these two-phase compositions, the power factor and ZT decrease in proportion to the indium concentration and they are consistent with mean field estimates based on the random distribution of two thermoelectric phases. Across the phase diagram, the electrical conductivity is n-type and the Seebeck coefficient is proportional to the natural logarithm of the electrical conductivity. Careful studies of electron mobility as a function of composition are clearly needed, especially electron transport across the InO_2 planes.

In closing, we believe that similar studies relating thermoelectric properties to phase equilibria are extremely useful in understanding and potentially identifying high temperature oxide thermoelectric materials. Very few semiconductor modular compounds have been studied to date but they have the potential for crystal engineering to independently modify both the electrical conductivity and thermal conductivity. Furthermore, there is also the possibility of altering, through doping, the density of states of the interfaces to alter the Seebeck effect and enhance ZT.

Acknowledgements

The authors are grateful to Dr M. Baram for assistance with the TEM and to the Center for Nanoscale Systems (CNS) at Harvard University for use of the microscopy facilities, a member of the National Nanotechnology Infrastructure Network (NNIN), which is supported by the National Science Foundation under NSF award no. ECS-0335765.

Appendix A. Conversion between molar and volume fractions

The mole fraction x of the component B can be written in terms of its volume fraction as follows:

$$x = \frac{\phi_B \frac{\rho_B}{M_B}}{\phi_B \frac{\rho_B}{M_B} + (1-\phi_B)\frac{\rho_A}{M_A}} \tag{19}$$

where ρ_i and M_i are the mass density and molecular weight of the each component.

For the In_2O_3 and $Zn_4In_2O_7$ two-phase composite system, we set In_2O_3 and $In_2O_3(ZnO)_4$ as component A and B, respectively. The $InO_{1.5} = 0.98$ sample with composition closest to the In_2O_3 end will represent the thermoelectric properties of In_2O_3. The corresponding mass density and molecular weights are as follows. For In_2O_3: $\rho_A = 7.179 \times 10^3$ g m^{-3} and $M_A = 277.64$ g mol^{-1}; for $Zn_4In_2O_7$: $\rho_B = 6.193 \times 10^3$ g m^{-3} and $M_B = 603.27$ g mol^{-1}. For the two-phase mixture of $Zn_7In_2O_{10}$ and $Zn_5In_2O_8$ superlattice compounds, we set $In_2O_3(ZnO)_4$ and $In_2O_3(ZnO)_5$ phases as component A and B, respectively, with their mass density and molecular weights as: for $k = 7$, $\rho_A = 6.034 \times 10^3$ g m^{-3} and $M_A = 847.26$ g mol^{-1};

for $k = 5$, $\rho_B = 6.126 \times 10^3$ g m^{-3} and $M_B = 684.50$ g mol^{-1}. The mass densities of $In_2O_3(ZnO)_4$, $In_2O_3(ZnO)_7$ and $In_2O_3(ZnO)_5$ were calculated based on the lattice parameter reported in the literature [16].

For the two-phase composite consisting of In_2O_3 and $In_2O_3(ZnO)_4$, the indium concentration can be further expressed in terms of mole fraction of component B as,

$$[In] = \frac{2x + 2(1-x)}{4x + 2x + 2(1-x)} \tag{20}$$

Similarly for the two-phase mixture of $In_2O_3(ZnO)_7$ and $In_2O_3(ZnO)_5$ superlattice compounds,

$$[In] = \frac{2x + 2(1-x)}{2x + 2(1-x) + 5x + 7(1-x)} \tag{21}$$

The above set of equations enables the two-phase composite thermoelectric power factor, which is originally expressed as a function of second-phase volume fraction, to be expressed and modeled as a function of indium concentration.

References

[1] Ohtaki M, Tsubota T, Eguchi K, Arai H. J Appl Phys 1996;79:1816.
[2] Tsubota T, Ohtaki M, Eguchi K, Arai H. J Mater Chem 1997;7:85.
[3] Cai KF, Muller E, Drasar C, Mrotzek A. Mater Sci Eng B – Solid State Mater Adv Technol 2003;104:45.
[4] Park K, Choi JW, Kim SJ, Kim GH, Cho YS. J Alloy Compd 2009;485:532.
[5] White MA, Ochsenbein ST, Gamelin DR. Chem Mater 2008;20:7107.
[6] Park K, Seong JK, Kim GH. J Alloy Compd 2009;473:423.
[7] Colder H, Guilmeau E, Harnois C, Marinel S, Retoux R, Savary E. J Eur Ceram Soc 2011;31:2957.
[8] Park K, Ko KY. J Alloy Compd 2007;430:200.
[9] Kishimoto K, Koyanagi T. J Appl Phys 2002;92:2544.
[10] Slack GA, Hussain MA. J Appl Phys 1991;70:2694.
[11] Koumoto K, Terasaki I, Funahashi R. MRS Bull 2006;31:206.
[12] Ohta H, Seo WS, Koumoto K. J Am Ceram Soc 1996;79:2193.
[13] Masuda Y, Ohta M, Seo WS, Pitschke W, Koumoto K. J Solid State Chem 2000;150:221.
[14] Hirano S, Isobe S, Tani T, Kitamura N, Matsubara C, Koumoto K. Jpn J Appl Phys Part 1 – Reg Pap Short Notes Rev Pap 2002;41:6430.
[15] Hopper EM, Zhu QM, Song JH, Peng HW, Freeman AJ, Mason TO. J Appl Phys 2011;109:6.
[16] Moriga T, Edwards DD, Mason TO, Palmer GB, Poeppelmeier KR, Schindler JL, et al. J Am Ceram Soc 1998;81:1310.
[17] Veblen DR. Am Mineral 1991;76:801.
[18] Snyder GJ, Toberer ES. Nat Mater 2008;7:105.
[19] Park K, Seong JK, Nahm S. J Alloy Compd 2008;455:331.
[20] McCoy MA, Grimes RW, Lee WE. J Mater Res 1996;11:2009.
[21] ICDD. PDF-4+ 2011 (Database). Newtown Square, PA, USA: International Centre for Diffraction Data; 2011.
[22] Barin I. Thermochemical data of pure substances. Weinheim: VCH; 1989.
[23] Qu XR, Wang W, Lv SC, Jia DC. Solid State Commun 2011;151:332.
[24] Bhosle V, Tiwari A, Narayan J. J Appl Phys 2006;100.
[25] Yamaguchi H, Chonan Y, Oda M, Komiyama T, Aoyama T, Sugiyama S. J Electron Mater 2011;40:723.
[26] Nakamura M, Kimizuka N, Mohri T. J Solid State Chem 1991;93:298.
[27] Nakamura M, Kimizuka N, Mohri T. J Solid State Chem 1990;86:16.
[28] Kimizuka N, Isobe M, Nakamura M, Mohri T. J Solid State Chem 1993;103:394.
[29] Uchida N, Bando Y, Nakamura M, Kimizuka N. J Electron Microsc 1994;43:146.
[30] Liang X, Baram M, Clarke DR. Appl Phys Lett 2013.
[31] Tritt TM. In: Clarke DR, Fratzl P, editors. Annual review of materials research, vol. 41; 2011. p. 433.
[32] Callaway J, von Baeyer HC. Phys Rev 1960;120:1149.
[33] Clarke DR. Surf Coat Technol 2003;163–164:67.
[34] Roufosse MC, Klemens PG. J Geophys Res 1974;79:703.
[35] Cahill DG, Pohl RO. Annu Rev Phys Chem 1988;39:93.
[36] McCoy MA, Grimes RW, Lee WE. Philos Mag A – Phys Condens Matter Struct Def Mech Prop 1997;76:1187.
[37] Harvey SP, Poeppelmeier KR, Mason TO. J Am Ceram Soc 2008;91:3683.
[38] Hopper EM, Zhu QM, Song JH, Peng HW, Freeman AJ, Mason TO. J Appl Phys 2011;109.
[39] Kimizuka N, Isobe M, Nakamura M. J Solid State Chem 1995;116:170.
[40] Nakamura M, Kimizuka N, Mohri T, Isobe M. J Solid State Chem 1993;105:535.
[41] Bergman DJ, Fel LG. J Appl Phys 1999;85:8205.
[42] Bergman DJ, Levy O. J Appl Phys 1991;70:6821.
[43] Nan CW, Birringer R, Clarke DR, Gleiter H. J Appl Phys 1997;81:6692.
[44] Kaga H, Asahi R, Tani T. Jpn J Appl Phys Part 1 – Reg Pap Short Notes Rev Pap 2004;43:3540.
[45] Ohtaki M, Ogura D, Eguchi K, Arai H. J Mater Chem 1994;4:653.
[46] Berardan D, Guilmeau E, Maignan A, Raveau B. Solid State Commun 2008;146:97.
[47] Liu Y, Lin Y-H, Lan J, Xu W, Zhang B-P, Nan C-W, et al. J Am Ceram Soc 2010;93:2938.
[48] Cheng B, Fang H, Lan JL, Liu Y, Lin YH, Nan CW. J Am Ceram Soc 2011;94:2279.
[49] Liu Y, Lin YH, Lan JL, Zhang BP, Xu W, Nan CW, et al. J Electron Mater 2011;40:1083.
[50] Park K, Seong JK, Kwon Y, Nahm S, Cho WS. Mater Res Bull 2008;43:54.
[51] Kazeoka M, Hiramatsu H, Seo WS, Koumoto K. J Mater Res 1998;13:523.